Long-term rogue wave occurrence probability from historical wave data on a spatial scale relevant for spar-type floating wind turbines

Nederkoorn, T. P.; Seyffert, H. C.

DOI
10.1016/j.oceaneng.2022.110955

Publication date
2022

Document Version
Final published version

Published in
Ocean Engineering

Citation (APA)
Nederkoorn, T. P., & Seyffert, H. C. (2022). Long-term rogue wave occurrence probability from historical wave data on a spatial scale relevant for spar-type floating wind turbines. *Ocean Engineering*, *251*, Article 110955. https://doi.org/10.1016/j.oceaneng.2022.110955

Ocean Engineering 251 (2022) 110955

Contents lists available at ScienceDirect

Ocean Engineering

journal homepage: www.elsevier.com/locate/oceaneng

Long-term rogue wave occurrence probability from historical wave data on a spatial scale relevant for spar-type floating wind turbines

T.P. Nederkoorn [a,b], H.C. Seyffert [a,*]

[a] Department of Maritime & Transport Technology, Delft University of Technology, The Netherlands
[b] INTECSEA, The Netherlands

ARTICLE INFO

Keywords:
Rogue waves
Historical wave data
Occurrence probability
Statistical wave models
Spar-type floating wind turbine
Dynamic response

ABSTRACT

Very large waves, such as rogue waves, can be dangerous for ships and offshore structures. There is no consensus on the theoretical occurrence probability of these rogues and ocean measurements containing rogue waves are rare. This paper addresses the long-term occurrence probability of rogue waves using time-extreme (TE) and space–time extreme (STE) statistical wave models, evaluated with a significant amount of historical directional wave data from Monterey Bay, California, USA. A novel understanding of these models is obtained by exploring the area size for which the STE models estimate a higher rogue wave occurrence probability compared to the TE models. For four rogue wave and crest heights the return periods until a 95% rogue wave occurrence probability are estimated. To illustrate an application of this statistical analysis, the risk of rogue waves to a spar-type floating wind turbine is evaluated. Based on both the dynamic response and the long-term occurrence probability of the rogue wave, this research presents a new and advanced approach for a risk analysis of rogue waves to floating offshore structures.

1. Introduction

Rogue waves, which are suddenly appearing, exceptionally large waves compared to the surrounding sea state, can pose a real threat to ships and offshore structures (Dysthe et al., 2008; Cavaleri et al., 2012). Assessing the occurrence probability of these extreme waves is important to better design offshore structures and increase safety. These rogue waves are often defined by two different size criteria: one relating to the crest height η_c (Eq. (1)) and the other to the wave height H (Eq. (2)) both normalized by the significant wave height H_s. These criteria must be met in a 20-min duration for the wave to be considered rogue (Haver, 2001; DNV, 2017). Here, H_s is taken as four times the standard deviation of the surface elevation (σ).

$$\frac{\eta_c}{H_s} \geq 1.25 \tag{1}$$

$$\frac{H}{H_s} \geq 2 \tag{2}$$

Different explanations for the generation mechanisms of rogue waves have been proposed, such as spatial and temporal wave focussing, wave blocking, and modulational instability, but so far no consensus has been reached (Dysthe et al., 2008). The EU project MaxWave set out to prove the existence of rogue waves and the risk of encounter (Rosenthal and Lehner, 2008). The MaxWave project, endorsed by other subsequent research, concluded that rogue waves occur more frequently than previously expected by conventional wave statistics (Fedele, 2012; Benetazzo et al., 2015).

However, as there is no consensus on the primary generation mechanism and since rogue waves are statistically rare events which are seldom physically measured, the occurrence probability of rogue waves remains unclear. Previous authors approached the occurrence probability by investigating characteristic wave parameters (Christou and Ewans, 2014; Cattrell et al., 2018) and meteorological conditions (Adcock et al., 2011; Cavaleri et al., 2016) in relation to rogue wave occurrences, but reported no quantitative statistics, though a recent investigation using significant amount of buoy data has suggested that the crest–trough correlation is an important parameter in rogue wave occurrence (Häfner et al., 2021). Surface kurtosis in relation to modulational instability was investigated as a rogue wave indicator (Mori and Janssen, 2006; Toffoli et al., 2015), but applicability to realistic ocean conditions has been questioned (Fedele et al., 2016; Benetazzo et al., 2017). In an intensive study by the CresT (Cooperative Research on Extreme Seas and their impacT) JIP that examined over 220,000 h of raw wave samples, the only resulting identifiable trend of rogue waves was frequency-phase focusing, perhaps caused by directional focusing (Christou and Ewans, 2011a,b). The authors found no discernible connection between rogue occurrence and sea state/ wave

* Corresponding author.
E-mail address: H.C.Seyffert@tudelft.nl (H.C. Seyffert).

https://doi.org/10.1016/j.oceaneng.2022.110955
Received 18 August 2021; Received in revised form 6 February 2022; Accepted 25 February 2022
Available online 17 March 2022

steepness, skewness, kurtosis, spectral shape, or environmental hindcast conditions based on wind, wave, and current data.

In this paper, the occurrence probability of different rogue waves is evaluated with multiple statistical wave models using historical wave buoy data. Both rogue wave definitions from Eqs. (1) and (2) are assessed separately, using wave crest and crest-to-trough models. The effect of including a spatial dimension in the probabilistic analysis is investigated by using both time-extreme (TE) statistical models, which consider extremes at a single point in time, and space–time extreme (STE) statistical models, which consider extremes over a given area in time. The area size from which an STE model yields a more conservative rogue wave estimate compared to a TE model is explored. This information is valuable when an offshore structure is considered and one wants to use the most conservative statistical wave model for extreme (rogue) wave analysis based on the footprint. Then, return periods until a 95% rogue wave occurrence probability are estimated for four rogue crest and wave heights. Lastly, an application of this probabilistic analysis is presented by evaluating the probability that rogue waves induce a damaging dynamic response in a spar-type floating wind turbine (SFWT). Spar-type floating wind turbines present an attractive and interesting option for analysis, considering the number of SFWTs already in-use the field and the many available open-source high-quality models.

This paper is structured as follows: Section 2 describes the considered statistical wave models used in the probabilistic analysis and introduces the directional wave data retrieved from the Monterey Bay wave buoy. Section 3 presents the method used to compare the statistical models and estimate the long-term rogue wave occurrence probability. Section 4 presents the results of the statistical analysis. In Section 5, an application of the statistical rogue wave analysis is presented by evaluating the risk of rogue waves to a SFWT. Finally, Section 6 presents the conclusions of this study.

Note that this paper examines time-extreme and space–time extreme wave crest and wave crest-to-trough models without considering the effects of wave breaking, as even the most extreme sea states examined here may be considered weakly nonlinear; interested readers may consider *e.g.*, Mori (2003), Latheef and Swan (2013), Karmpadakis et al. (2019) and Schubert et al. (2020) for more in-depth discussions on such effects.

2. Utilized models & data

2.1. Statistical wave models

The two rogue wave definitions regarding the crest height, Eq. (1), and the crest-to-trough height, Eq. (2), are evaluated separately. Two statistical approaches are used: the first concerns the surface elevation at a fixed point in time, called time-extreme models (TE), and the second concerns the sea surface elevation over an area ($X \times Y$ m^2) in time, called space–time extreme models (STE). The statistical models used for this purpose are briefly introduced below and are presented in more detail in the Appendix.

2.1.1. Wave crest models

Realistic ocean waves are characterized by steeper crests and shallower troughs compared to the linear shape. The wave crest height is affected by surface nonlinearities which increases the probability of a large wave crest occurring beyond that estimated by the linear Rayleigh model (Holthuijsen, 2007). Weibull-type distributions which incorporate second-order surface nonlinearities, such as those from Tayfun (1980) and Forristall (2000), are considered to provide a good estimate of the crest height at a fixed point in time (*i.e.*, as a TE model) (Dysthe et al., 2008; Casas-Prat and Holthuijsen, 2010). Tayfun and Fedele also presented an extension of the Tayfun model to incorporate third-order nonlinearities by taking the excess kurtosis of the wave field into account (Tayfun and Fedele, 2007).

Research has shown that maximum crest heights evaluated over an area of size $X \times Y$ m^2 are generally larger than those at a fixed point (Krogstad et al., 2004; Fedele, 2012; Benetazzo et al., 2015). Fedele, drawing upon Adler and Taylor (2009), presented a linear space–time extreme statistical wave model, hereafter referred to as the STE1 model (Fedele, 2012). Benetazzo et al. extended the linear space–time model using the nonlinear Tayfun crest definition, resulting in a nonlinear STE model (Benetazzo et al., 2015), hereafter referred to as STE2.

2.1.2. Wave crest-to-trough models

Crest-to-trough heights are only slightly affected by surface nonlinearities. Wave heights can be predicted by the Rayleigh distribution (Longuet-Higgins, 1952), but observations have shown that the Rayleigh model slightly over-predicts the wave heights (see, *e.g.,* McAllister and van den Bremer (2020)). A bandwidth-corrected Rayleigh model, such as presented by Naess (1985), results in a more accurate estimation (Casas-Prat and Holthuijsen, 2010). A crest-to-trough STE probability model is formulated by extending the STE1 model with the quasi-determinism theory from Boccotti (2000). This theory states that the largest waves in a wave spectrum follow a deterministic shape based on the autocorrelation function of the underlying wave energy spectrum, thus giving a relation of crest height to wave height. This linear extended crest-to-trough STE model will be referred to as the STE1QD model.

2.2. Environmental wave data

This research considers directional wave data from the Monterey Bay wave buoy (see Fig. 1), operated by the National Buoy Data Center (NBDC). Wave data is available from June 1998 until the end of 2020, which is a significant amount considering the life of a typical offshore structure (Ersdal and Hörnlund, 2008).

The wave data of the NDBC buoys is not acquired from direct measurements. Accelerometers or inclinometers within the buoy measure the heave acceleration or the vertical displacement of the hull during a 20-min data acquisition window in each hour, together with sensors such as a triaxial magnetometer and/or three orthogonal angular rate sensors, which measure the hull azimuth, pitch, and roll angles. Then this data is transformed from the time domain to the frequency domain by applying a Fast Fourier transformation. After this transformation, response amplitude operator processing is performed on the data to eliminate hull and electronic noise so that the directional and non-directional wave parameters can be derived.

The buoy output is associated with six different data files, which are sampled for each hourly record (based on the representative 20-min acquisition window) and collected per year. The measurements taken during the 20-min data acquisition window are assumed to represent the conditions for the whole hour. The first file contains meteorological data such as wind speed, significant wave height, dominant wave period, air pressure, etc. The second file contains the wave energy in m^2/Hz. The third until sixth file contain parameters necessary to calculate the directional wave spectrum sampled per frequency: mean wave direction, principal wave direction, and two Fourier constants.

Corrupt hourly entries, where for any of the above parameters a value is *e.g.*, missing, not a number, or an unreasonably high/low number are identified and filtered out by complete removal of the corresponding time stamp in all data files. After filtering, a total of 19.5 years (170,845 hourly sea states) of usable wave data is obtained.

A directional wave spectrum can be represented using the directional Fourier series expansion (Longuet-Higgins, 1961) based on the buoy parameters θ_1 = mean wave direction, θ_2 = principal wave direction, r_1 = first normalized directional Fourier constant, r_2 = second normalized directional Fourier constant, and $C_{11}(f)$ = non-directional

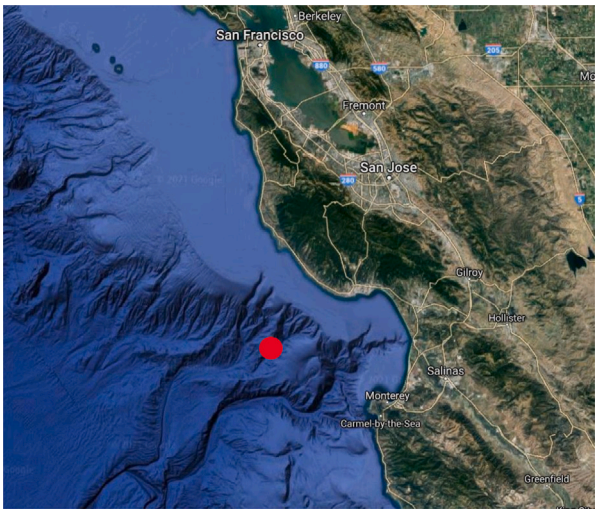

Fig. 1. Location of the Monterey Bay directional wave buoy. Water depth: 1646 m. (Google maps, 2021).

spectral density (energy). Using the directional Fourier series expansion, the wave spectrum $S(f,\theta)$ can be written as:

$$S(f,\theta) = C_{11}(f)D(f,\theta) \tag{3}$$

$D(f,\theta)$ is the directional spreading function without any weighting values to prevent negative energy:

$$D(f,\theta) = \frac{\frac{1}{2} + r_1 \cos\left(\theta - \theta_1\right) + r_2 \cos\left(2\left(\theta - \theta_2\right)\right)}{\pi} \tag{4}$$

The weighting values can be added in an analogous manner to the cosines of Eq. (4). Weighting values are needed because co- and cross-spectra from three-dimensional buoy data can only resolve the first five terms in the directional Fourier series expansion. Therefore, higher terms are usually considered zero. However, this can introduce negative spectral energy in some frequency bands; this is often counteracted by the addition of weighting values to the terms in Eq. (4) (Longuet-Higgins, 1961). For this investigation they are chosen as $\frac{2}{3}$ and $\frac{1}{6}$ for the first and second cosine respectively, after Earle et al.. Other approaches to deal with this negative-energy issue are addressed by Gorman (2018).

3. Methods

The input parameters for the statistical wave models (see Table 1) follow from the spectral directional moments. For each hourly sea state, the directional wave spectrum is calculated using Eq. (4), and the spectral moments are numerically evaluated by Eq. (5).

$$m_{ijk} = \iint k_x^i k_y^j f^k S(f,\theta) df d\theta \tag{5}$$

Here k_x and k_y are the directional wave number in the $x-$ and $y-$direction, respectively, f the wave frequency and $S(f,\theta)$ the directional wave spectrum. The buoy provides directional wave data in degrees, measured clockwise from true north. The main direction of wave propagation is chosen as the direction of the positive x-axis when calculating the spectral directional moments.

The statistical models are evaluated in each hourly sea state for either the rogue crest, or the rogue crest-to-trough threshold definition. The rogue crest definition from Eq. (1) is reformulated by normalizing the wave crest elevation with the standard deviation of the sea surface (σ). The significant wave height is assumed equal to 4σ, resulting in the new rogue crest definition $\eta_{rogue}/\sigma \geq 5$. The exceedance probability of the rogue threshold is calculated over a period of 20 min to comply with the rogue definitions (Haver, 2001; DNV, 2017) based on the 20-min data acquisition period representing each hour.

Table 1
An overview of the considered statistical wave models.

Probability model	Time-extreme (TE)	Space–time extreme (STE)
Crest	Forristall (2000) Tayfun (1980) Tayfun and Fedele (2007)	STE2 (Benetazzo et al., 2015)
Crest-to-trough	Naess (1985) Longuet-Higgins (1952)	STE1QD (Boccotti, 2000)

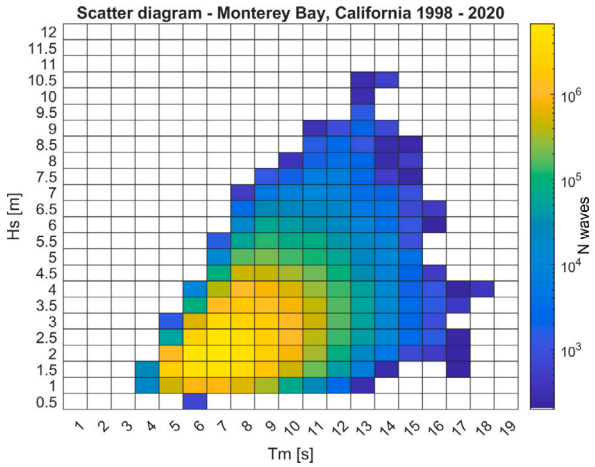

Fig. 2. Scatter diagram of the significant wave height and the mean zero-crossing wave period.
Source: Dataset from Monterey Bay from 1998–2020.

According to Benetazzo et al., the area evaluated with the STE models should be smaller than 100×100 m^2 for the unbounded STE models to stay accurate and prevent theoretical unlimited growth (Benetazzo et al., 2020). Therefore, the STE models are evaluated in the range of no spatial component ($X = 0, Y = 0$), to an area of $XY = 100 \times 100$ m^2.

3.1. Wave climate

Fig. 2 gives the average number of waves (N) in each sea state, calculated using the mean zero-crossing wave period, T_m. From this diagram, frequently occurring combinations of H_s and T_m are chosen as criteria to compare the models on. Also, this diagram is used to address the occurrence probability of certain sea states.

3.2. Long-term rogue probability

To estimate the long-term rogue probability, both the short-term rogue statistics and the sea state occurrence probability have to be taken into account. In Fig. 2, the wave climate is visualized by a scatter diagram displaying the average number of waves in bins of significant wave height and mean zero-crossing period. For the purpose of calculating the overall rogue probability, this scatter diagram is slightly modified to consider the number of 1-h sea states in each bin.

Four rogue size thresholds are established for both the crest and the crest-to-trough height. Since only very large waves are relevant for the safety of offshore structures, the four uppermost rows containing entries in Fig. 2 are investigated. For each of these rows, the average significant wave height is calculated to serve as a benchmark for the thresholds. Table 2 presents these H_s averages, together with the corresponding rogue thresholds.

Each bin of Fig. 2 is evaluated separately in terms of its exceedance probability of the rogue thresholds during the duration $D = 1200$ s,

Table 2
Average significant wave height and corresponding rogue thresholds of the four rows containing the highest sea states of the scatter diagram.

Scatter diagram row H_s [m]	Avg H_s [m]	η_{rogue} [m]	H_{rogue} [m]
10–10.5	10.31	12.89	20.62
9.5–10	9.92	12.40	19.84
9–9.5	9.13	11.41	18.26
8.5–9	8.78	10.98	17.56

$P(\eta/\sigma \geq \xi \mid D)$ and $P(H/H_s \geq z \mid D)$. First, the average H_s of the sea states within that bin is calculated. This average H_s is then used to determine the average threshold ξ or z that a sea state within that particular bin will have to exceed the rogue thresholds. Using these ξ and z values, an average exceedance probability is calculated per bin. This is done by taking the average of the exceedance probabilities of all the sea states within the bin evaluated at that average ξ or z value.

To calculate the probability that at least one wave in the dataset exceeds one of the thresholds, instead the null problem is considered: the probability that no wave in the dataset exceeds one of the thresholds (see Eq. (6)). Here the sea states, Ss_i are assumed to be statistically independent.

$$\mathrm{P(rogue)} = 1 - \left(\bigcap_{i=1}^{N} \mathrm{P(no\ rogue} \mid \mathrm{Ss_i}) \right) \tag{6}$$

$\mathrm{P(no\ rogue} \mid \mathrm{Ss_i})$ is defined as the average probability of no wave exceeding the rogue threshold in that particular sea state (Ss_i), to the power K, which represents the number of 20-min time series expected for that sea state, based on the scatter diagram in Fig. 2:

$$\mathrm{P(no\ rogue} \mid \mathrm{Ss_i}) = \mathrm{P(no\ rogue)}_{\mathrm{i,avg}}^{\mathrm{K}} \tag{7}$$

Sea states are excluded from the calculation based on two criteria: (1) if the average wave has a negligible probability of being considered rogue in that particular sea state, or (2) if the wave breaking limit evaluated using the average mean zero-crossing period ($H/L < 0.14$) is exceeded (Holthuijsen, 2007).

For the first criterion, note that of course each of the sea states from Fig. 2 could theoretically exceed one of the rogue wave thresholds defined in Table 2, given enough time. But in low sea states, the threshold ξ and z which have to be exceeded in order to produce a rogue wave large enough to surpass the thresholds established in Table 2 will be much higher compared to those of a high sea state. The probability of exceeding a high threshold ξ and z rapidly decreases as the threshold increases. This means that, having the scatter diagram in mind, from a certain sea state range downwards, the contribution of those low sea states to the exceedance probability of the rogue thresholds is negligible. Conversely, note that only waves which classify as rogue are of interest to this calculation. If in a sea state the threshold ξ and z is not considered rogue, then that sea state is excluded from the calculation.

Considering the second criterion, since the wave breaking limit is defined with respect to the wave height and not the crest height, the rogue wave height from Table 2 is used to determine the wave breaking limit belonging to the corresponding rogue crest height. At some point, sea states will be excluded from the calculation if the wave breaking limit $H/L < 0.14$ is exceeded (Holthuijsen, 2007). To give a quick indication of this cut-off limit the lowest crest-to-trough threshold of Table 2, $H_{rogue} = 17.56$ m, is taken as an example. The minimum wavelength which a wave should have in order to attain such a wave height and not break would be ~125 m. Using the deep-water dispersion relationship, this corresponds to a minimum wave period of ~9 s. For each bin this wave breaking limit is evaluated using the average mean zero-crossing period. Since the wave breaking limit is defined with respect to the wave height and not the crest height, the rogue wave height from Table 2 is used to determine the wave breaking limit belonging to the rogue crest height in the same row as well.

Table 3
10 chosen sea state bins spanning possible range of H_s values.

H_s range	T_m range
$1 < H_s \leq 1.5$ m	$6 < T_m \leq 7$ s
$2 < H_s \leq 2.5$ m	$6 < T_m \leq 7$ s
$3 < H_s \leq 3.5$ m	$7 < T_m \leq 8$ s
$4 < H_s \leq 4.5$ m	$7 < T_m \leq 8$ s
$5 < H_s \leq 5.5$ m	$8 < T_m \leq 9$ s
$6 < H_s \leq 6.5$ m	$8 < T_m \leq 9$ s
$7 < H_s \leq 7.5$ m	$10 < T_m \leq 11$ s
$8 < H_s \leq 8.5$ m	$11 < T_m \leq 12$ s
$9 < H_s \leq 9.5$ m	$12 < T_m \leq 13$ s
$10 < H_s \leq 10.5$ m	$13 < T_m \leq 14$ s

These two exception criteria for the rogue calculation are linked for the exclusion of sea states. By considering the wave period cut-off limit for wave breaking, an assumption can be made from which point the inclusion of low sea states in the overall rogue wave probability calculation becomes insignificant. Since the lowest rogue wave threshold requires a minimum wave period of ~9 s, we can disregard all bins containing waves with a lower mean zero-crossing period. The largest amount of sea states found in one bin in the valid T_m range then becomes '2758' (bin $2 < H_s \leq 2.5$ & $9 < T_m \leq 10$). Following Eq. (7), this would lead to $K_{max} = 8274$ time records. Once the largest average sea state exceedance probabilities $P(no\ rogue)_{i,avg}$ are found to be in the order of 10^{-9}, the inclusion of lower sea states are disregarded. Even using the value K_{max}, this would no longer significantly influence the overall rogue probability.

4. Rogue wave occurrence probability analysis

This section presents the results of the rogue wave occurrence probability analysis. First, the area from which the STE models estimate a higher rogue wave probability than the TE models is investigated. This is done by comparing the TE and STE models to each other based on their estimated probability of exceeding the rogue threshold in different sea states for a range of area sizes. Then return periods until a 95% occurrence probability are reported for four different size rogue waves.

4.1. Influence of spatial scale on predicted rogue wave probability

The TE and STE models are compared in 10 different sea state combinations of H_s and T_m, based on Fig. 2. Note that an in-depth explanation of the TE models is given in the Appendix Sections A.1 and A.2, while the STE models are further described in the Appendix Sections A.3 and A.4.

Frequently occurring sea states are identified for each possible H_s range of Fig. 2 (such as $2 < H_s \leq 2.5$ m) by selecting the modal period T_m bin for a given H_s range containing the largest number of expected waves (N). With 21 rows containing entries, this results in 21 sea state bins. Then, from those frequently occurring combinations, 10 evenly spaced bins over the H_s range are chosen as the sea states to compare the models in as given in Table 3.

The STE and TE models are compared based on their estimated exceedance probability of the rogue threshold (Eq. (1)–(2)) within 20 min. In each of the 10 sea state bins, the maximum probability of exceeding the rogue threshold is identified for each wave model. These are the highest probabilities per bin and are chosen as a way to represent a worst-case scenario in terms of rogue wave occurrence. The probability estimated by an STE model is divided by that of a TE model, in a range starting from no spatial component ($X = 0, Y = 0$) to $XY = 100 \times 100$ m^2, in each of the 10 sea states. This results in a ratio of "STE over TE" for different area sizes, facilitating a simple comparison.

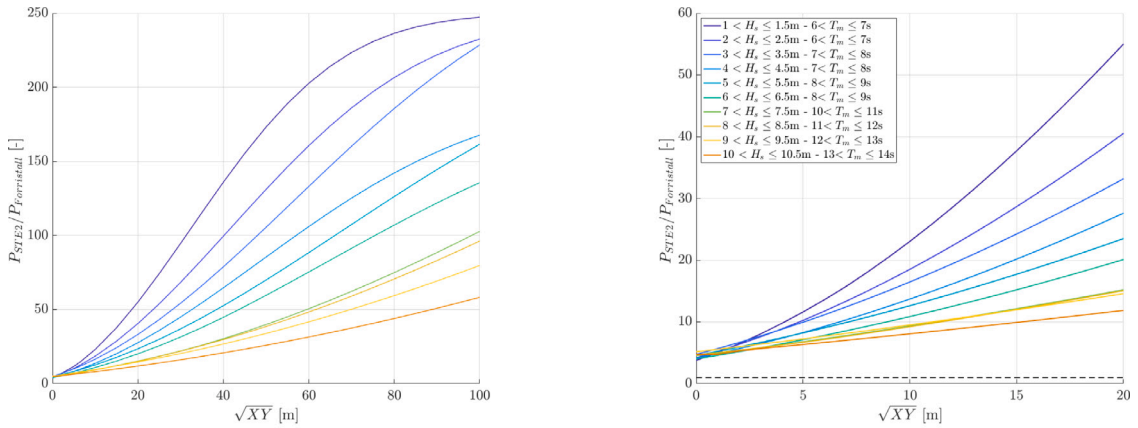

(a) (b)

Fig. 3. Comparison of the STE2 (Benetazzo et al., 2015) and TE Forristall (Forristall, 2000) estimate of $P(\eta_{max}/\sigma \geq 5 \mid \mathrm{D})$ with D = 1200 s. (a) Area sizes ranging from no spatial component ($X = 0, Y = 0$) to 100×100 m^2. (b) Area sizes ranging from no spatial component ($X = 0, Y = 0$) to 20×20 m^2. The horizontal black dashed line visualizes a y-ratio of 1 .

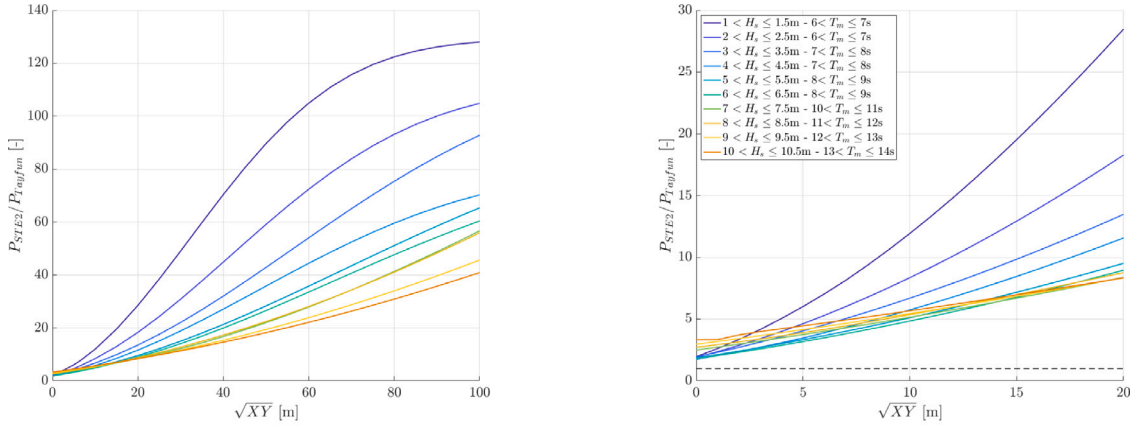

(a) (b)

Fig. 4. Comparison of the STE2 (Benetazzo et al. (2015)) and TE Tayfun (Tayfun, 1980) estimate of $P(\eta_{max}/\sigma \geq 5 \mid \mathrm{D})$ with D = 1200 s. (a) Area sizes ranging from no spatial component ($X = 0, Y = 0$) to 100×100 m^2. (b) Area sizes ranging from no spatial component ($X = 0, Y = 0$) to 20×20 m^2. The horizontal black dashed line visualizes a y-ratio of 1.

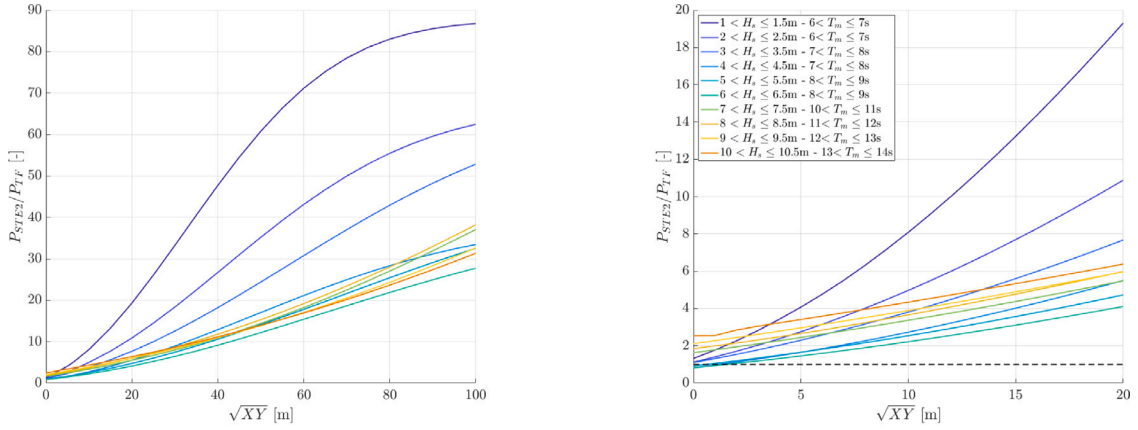

(a) (b)

Fig. 5. Comparison of the STE2 (Benetazzo et al. (2015)) and TE Tayfun–Fedele (Tayfun and Fedele, 2007) estimate of $P(\eta_{max}/\sigma \geq 5 \mid \mathrm{D})$ with D = 1200 s. (a) Area sizes ranging from no spatial component ($X = 0, Y = 0$) to 100×100 m^2. (b) Area sizes ranging from no spatial component ($X = 0, Y = 0$) to 20×20 m^2. The horizontal black dashed line visualizes a y-ratio of 1.

4.1.1. Wave crest models

Figs. 3, 4 and 5 present the comparisons between the STE2 model from Benetazzo et al. and the TE Forristall, Tayfun, and Tayfun–Fedele models respectively. The area size is reported on the x-axis in terms of $\sqrt{XY}$ as a way to specify the length of the sides of the square area. The values on the y-axis represent the ratio of the exceedance probability estimated by the STE model to that of the TE model. Some observations regarding these figures:

- As the area size of the STE2 model increases, the relative difference between the rogue crest threshold exceedance probabilities estimated by the TE and STE models increases.
- Regarding the TE models, the Forristall model appears to estimate the lowest rogue crest threshold exceedance probabilities, followed by the Tayfun model. The Tayfun–Fedele model estimates the highest exceedance probabilities for these TE crest models.
- Figs. 3 and 4 clearly show a decreasing trend of the relative difference between the estimated rogue crest threshold exceedance probability by the STE and TE model, as the sea state trends to higher H_s values. This decreasing trend can be explained by the fact that as waves become higher, they generally become longer crested, thus decreasing the number of unique waves that exist within or on the borders of the considered area and therefore decreasing the influence of the spatial dimension, as also suggested by Fedele (2012).
- A similar conclusion was noted by Barbariol et al. when comparing time-extreme (Forristall) and space–time extreme (STE2) estimates from reanalysis datasets (validated based on buoy and stereo-video wave observations for the TE and STE models, respectively) (Barbariol et al., 2019). They found that for a single fixed area (100×100 m^2), more extreme conditions (99th percentile) were associated with longer wavelengths than typical conditions (50th percentile), making the statistical effects of the 3D geometry of waves and their short-crestedness less pronounced. Figs. 3 and 4 further indicate that the effects of a diminishing spatial component (*i.e.*, smaller area size within the STE model) have a more drastic impact on moderate sea states than extreme sea states.
- Note that larger H_s values are also associated with larger T_m values as well, meaning that these higher sea states may also have fewer unique waves within some considered area due to longer wave periods. The STE models take this into account by calculating the average number of waves expected along the one-dimensional spatial perimeter of the area boundary, N_B (Eq. (A.16)), on the two-dimensional spatial surfaces, N_S (Eq. (A.17)), and within the three-dimensional space–time domain, N_V (Eq. (A.18)) over some time duration D, where all these numbers of waves decrease for increasing wave period T_m. This reduced number of waves reduces the exceedance probabilities for both the STE1 and STE2 model, Eq. (A.30)–(A.31).
- Wave spreading can also play a role here. Latheef and Swan note that when considering the role of directional spreading in physical experiments, unidirectional situations show the largest nonlinear amplifications to wave crest measurements, though this effect seems to reduce for steeper sea states where wave breaking may play a role (Latheef and Swan, 2013); this result was also confirmed by numerical simulations of the Euler equation (Toffoli et al., 2008). More unidirectional sea conditions may also lead to more long-crested waves, suggesting larger nonlinear amplifications of wave crests. However, this effect is also closely intertwined with wave breaking and steepness which may counteract such effects; unraveling the overall outcome of such dependent effects is therefore beyond the scope of this paper.
- Fig. 5 also shows traits of the above mentioned trend, though it is less pronounced. Many of the curves in Fig. 5, from a sea state of $4 < H_s \leq 4.5$ m and higher, are somewhat clustered together. This could be explained due to the fact that the Tayfun–Fedele model is an extension of the Tayfun model where an extra parameter, the excess kurtosis, is taken into account to incorporate third order surface nonlinearities.

Notice that as the area sides X and Y approach 0 m, the STE2 model still approximates higher probabilities of a rogue crest threshold exceedance than the Forristall and Tayfun model. This can clearly be observed via the black dashed line which denotes the ratio threshold of 1, indicating whether the STE or TE model estimates a higher probability, visible in Figs. 3(b) and 4(b). From an analytical point of view, one might expect the STE2 and Tayfun model to converge at $\sqrt{XY} = 0$ m, since the Tayfun crest definition was used to extend the linear STE1 model to the nonlinear STE2 model. However, when formulating the exceedance probability function of the STE models, the asymptotic Gumbel limit was used to ensure probabilities bounded by 1 for small η/σ thresholds (Fedele, 2012; Benetazzo et al., 2015). Therefore these two models do not converge as the area sides X and Y approach 0.

Only the Tayfun–Fedele model, in two sea states, slightly estimates a higher rogue crest threshold exceedance probability than the STE2 model as the area sides X and Y approach 0. However, this difference can be considered insignificant, as from an area of approximately 2×2 m^2 onwards the STE2 model again predominates. Since this area can be considered small, and the Tayfun–Fedele model is the most conservative TE wave crest model, one can conclude that when rogue wave crests are considered for structures like floating offshore wind turbines, inclusion of the spatial dimension using the STE2 model from Benetazzo et al. (2015) will provide the most conservative estimate in all sea states.

4.1.2. Wave crest-to-trough models

Figs. 6 and 7 present the comparisons of the STE1QD model from Boccotti with the TE Naess and Rayleigh model respectively. The increasing difference in estimated rogue crest-to-trough threshold exceedance probability between the STE and TE models is again clearly visible as the area increases, as well as the declining relative difference as the sea state becomes higher. Note that both in Figs. 6 and 7 the lines corresponding to the two lowest sea states seem to approach a maximum as the area increases. This is because in those sea states, the STE1QD model estimates an exceedance probability of almost 1 from a certain area size onwards.

Fig. 6(b) shows that as the area sides X and Y decrease to 0, the STE1QD model still predominates the Naess model. It can be observed in Fig. 7(b) that for a small area (approximately $< 2 \times 2$ m^2), the Rayleigh model always estimates a higher rogue wave crest-to-trough threshold exceedance probability than the STE1QD model, regardless of the sea state. As the area size increases, the STE1QD model starts to predominate, and from an area size of around 12×12 m^2 onwards the STE1QD model estimates higher probabilities even in the highest sea states. This is interesting because the Rayleigh model is generally regarded to overestimate wave heights. These results indicate that when rogue waves are evaluated for an offshore structure with a footprint larger than 12×12 m^2, inclusion of the spatial dimension using the STE1QD model from Boccotti (2000) will provide the most conservative occurrence estimate of rogue crest-to-trough threshold exceedance probabilities in all sea states.

4.1.3. Wave crest vs. crest-to-trough models

One thing is clear from comparing the STE/TE ratios from the wave crest models (Figs. 3, 4, 5) and from the wave crest-to-trough models (Figs. 6, 7): the wave crests seem to be more affected by the spatial component than do the wave crests-to-troughs. To understand this difference, we look to studies comparing such STE and TE models with more detailed wave observation measurements. Barbariol et al. noted that the STE2 wave crest model extended with quasi-determinism theory, which accounts for second-order non-resonant wave non-linearities, better matched the temporal profiles for the largest wave crest heights from stereo video measurements than the linear STE1QD model. They also noted that the time-extreme wave crest Tayfun–Fedele model overestimated wave crests, while the time-extreme wave crest-to-trough Naess model slightly underestimated these crest-to-trough heights as compared to buoy measurements. When comparing the space–time extreme models to the time-extreme models, Barbariol et al. similarly found that the wave crests were more affected by the addition of the spatial component (*i.e.*, larger estimates) than were the wave crest-to-troughs (Barbariol et al., 2019).

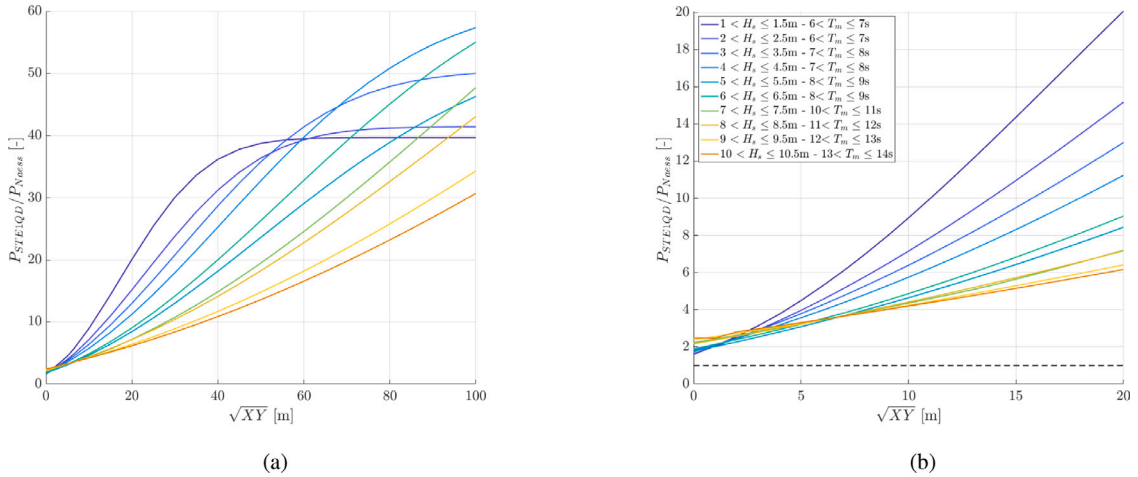

Fig. 6. Comparison of the STE1QD (Boccotti, 2000) and TE Naess (Naess, 1985) estimate of $P(H_{max}/H_s \geq 2|\mathrm{D})$ with D = 1200 s. (a) Area sizes ranging from no spatial component $(X = 0, Y = 0)$ to 100×100 m^2. (b) Area sizes ranging from no spatial component $(X = 0, Y = 0)$ to 20×20 m^2. The horizontal black dashed line visualizes a y-ratio of 1.

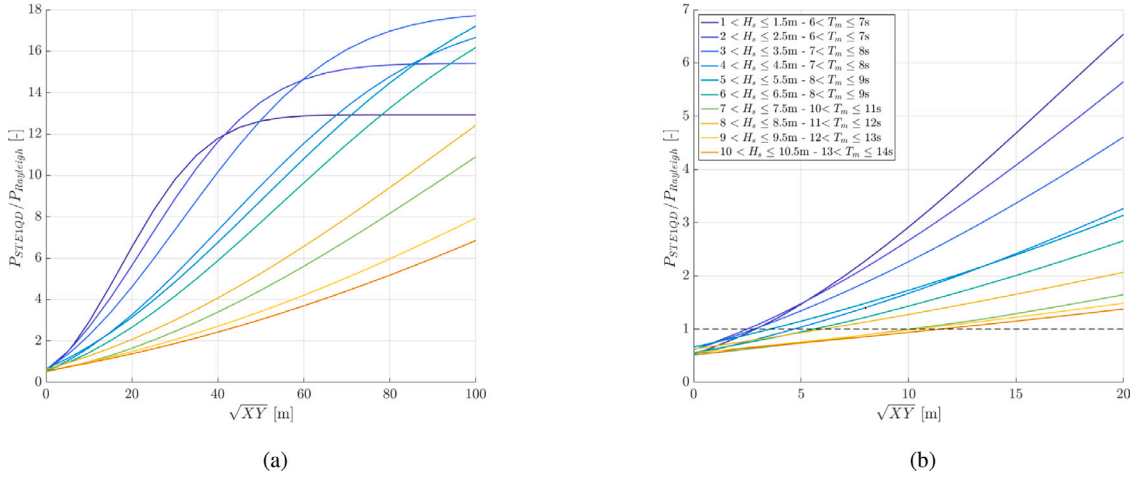

Fig. 7. Comparison of the STE1QD (Boccotti, 2000) and TE Rayleigh estimate of $P(H_{max}/H_s \geq 2|\mathrm{D})$ with D = 1200 s. (a) Area sizes ranging from no spatial component $(X = 0, Y = 0)$ to 100×100 m^2. (b) Area sizes ranging from no spatial component $(X = 0, Y = 0)$ to 20×20 m^2. The horizontal black dashed line visualizes a y-ratio of 1 .

4.2. Long-term rogue probability

Now the long-term rogue wave occurrence probability according to the different statistical models is investigated in terms of a return period until the rogue threshold exceedance probability is at least 95%. The wave climate suggested by the Monterey Bay buoy data, visualized by Fig. 2, is extrapolated for this purpose. Tables 4 and 5 present these return periods for the four considered rogue crest and wave heights. To reflect the footprint of an offshore structure, the area sides X and Y of the STE models are defined using the waterline diameter (6.5 m) of a reference SFWT model developed for phase IV of the IEA Offshore Code Comparison Collaboration (OC3) (Jonkman, 2010), hereafter referred to as the OC3-Hywind concept.

For the considered rogue crests, the Forristall model estimates the longest return periods, followed by the Tayfun model, then by the Tayfun–Fedele model, while the STE2 model from Benetazzo et al. estimates the lowest return periods. The difference between the Tayfun–Fedele model and the STE2 model is significant, which was expected regarding the earlier results from Section 4.1.1. In offshore design practices it is common to work with 50- and 100-year return periods for extreme environmental conditions (DNV, 2017). The return periods estimated by the TE models all largely exceed 100 years. Only the STE2 model estimates return periods lower than 100 years for the two smallest rogue crests. This illustrates how using an STE model could provide more conservative estimates than a TE model.

Between the crest-to-trough models it is observed that the Rayleigh and STE1QD model from Boccotti estimate lower return periods than the Naess model. During the model comparisons of maximum rogue crest-to-trough threshold exceedance probabilities, it was observed that up until an area size of 12×12 m^2, the Rayleigh model estimated higher rogue wave probabilities in several sea states. In this long term rogue probability calculation, the results indicate that for the considered area of 6.5×6.5 m^2, the Rayleigh and STE1QD model estimate similar occurrence probabilities. For the two smallest rogue wave thresholds, these periods are very close and for the two largest waves the STE1QD model is slightly more conservative. When the overall rogue wave probability is considered, it appears that the STE1QD model is already more conservative from an area size of 6.5×6.5 m^2.

Note that in some cases the return periods in the third column (second rogue threshold) are higher than those in the fourth column (first rogue threshold). This is due to the exclusion of sea states in which a certain rogue threshold is not considered rogue. By raising the threshold, more sea states are included which in this case reduces the return period relative to the previous column.

Of course, it is important to note that these estimations assume independent sea states and do not account for temporal variability in sea conditions. Seasonal variability may introduce important effects, as noted by Cattrell et al., who found rogue wave intensification trends during winter periods when analyzing different Southern California buoy data (Cattrell et al., 2019).

Table 4
Return periods in years necessary until the rogue threshold exceedance probability is at least 95%, per threshold, for the Forristall, Tayfun, Tayfun–Fedele and STE2 model.

Probability of *at least one* rogue wave Return period until 95% probability	η_{rogue} = 10.98 m [years]	η_{rogue} = 11.41 m [years]	η_{rogue} = 12.40 m [years]	η_{rogue} = 12.98 m [years]
Forristall (2000)	750	1000	5000	3350
Tayfun (1980)	400	525	2400	2150
Tayfun and Fedele (2007)	175	235	960	1010
STE2 6.5 × 6.5 m^2 (Benetazzo et al., 2015)	55	72	230	260

Table 5
Return periods in years necessary until the rogue threshold exceedance probability is at least 95%, per threshold, for the Naess, Rayleigh and STE1QD model.

Probability of *at least one* rogue wave Return period until 95% probability	H_{rogue} = 17.56 m Years	H_{rogue} = 18.26 m Years	H_{rogue} = 19.84 m Years	H_{rogue} = 20.62 m Years
Naess (1985)	123	180	850	660
Rayleigh (Longuet-Higgins, 1952)	22	33	147	134
STE1QD 6.5 × 6.5 m^2 (Boccotti, 2000)	22	31	104	113

5. Application: spar-type floating wind turbine response to rogue wave impact

To illustrate an application of this statistical rogue wave analysis, a risk analysis is done by evaluating the dynamic response of a spar-type floating wind turbine (SFWT) to the four considered rogue waves in Table 2. A frequently used concept for such research is the OC3-Hywind concept from Jonkman et al. (2009) and Jonkman (2010).

Limited research has been done on the response of a SFWT to a single rogue wave. Ruzzo and Arena analyzed the dynamic response of a SFWT (OC3-Hywind) to a single rogue wave using a 3-DOF in-house numerical code (Ruzzo and Arena, 2019). Qu et al. investigated the effect of the wave–current interaction on the generation process of a rogue wave and evaluated the dynamic response of the SFWT (OC3-Hywind) using a 6-DOF in-house numerical code (Qu et al., 2020). Both papers considered one size rogue wave, limited to one sea state, where nothing about the rogue wave statistics or their severity could be concluded for realistic ocean conditions. The statistical rogue wave analysis allows this paper to assess the possible danger of a rogue wave to a SFWT with a clear connection to occurrence probability and return period.

5.1. Deterministic rogue wave time series

For this research, wave time series with a deterministic rogue wave are generated based on the NewWave theory (Tromans et al., 1991). Taylor et al. introduced a method to embed the NewWave profile in a stochastic wave time series (Taylor et al., 1997). Their method ensures a deterministic extreme wave at time t_r, after which the wave series returns to the random shape of the background waves, which is referred to as the most-likely wave (MLW) model.

For each sea state bin included in Table 2 a 'most-likely wave spectrum' is estimated. This most-likely wave spectrum aims to reflect the average of the sea states in which that particular size rogue wave is most likely to occur. An assumption is made that the most-likely wave spectrum consists of the averaged wave spectrum belonging to the scatter diagram row of that particular rogue wave threshold, together with two rows below (see Fig. 8). These resulting most-likely wave spectra are defined in Table 6. The random wave time series were generated from these most-likely wave spectra.

Due to the influence of the underlying wave spectrum moving away from the deterministic wave peak at the defined point of interest, the preceding and following wave trough around the rogue event are influenced. To give similar rogue wave crest-to-trough conditions for multiple simulations for each rogue wave height threshold, the crest amplitude was iteratively adjusted to ensure the resulting crest-to-trough height, when embedded in the random time series, met the desired H_{rogue} criterion.

Table 6
Significant wave height H_s and peak modal period T_p for the most-likely wave spectrum associated with each rogue threshold. The average rogue wave period, rogue wave steepness ($H_{rogue}/\lambda_{rogue}$), and wave spectrum steepness ($\frac{1}{2}H_s k_p$) are also given for each rogue height.

H_{rogue} [m]	H_s [m]	T_p [s]	Rogue period [s]	Rogue steepness [−]	Sea state steepness [−]
20.62	8.93	19.23	15.67	0.0538	0.0486
19.84	8.92	17.24	15.57	0.0524	0.0604
18.26	8.55	16.94	15.3	0.0500	0.0600
17.56	8.16	16.94	14.3	0.0550	0.0572

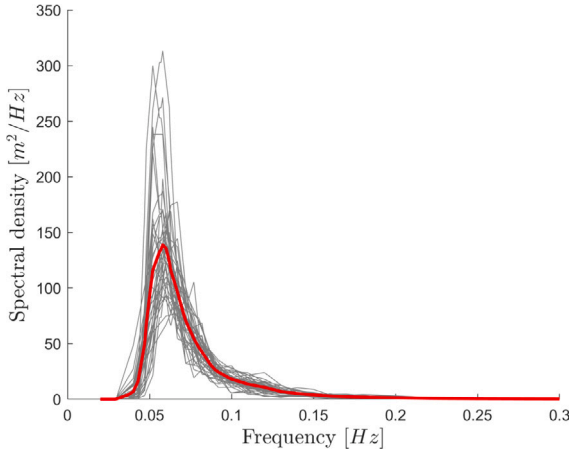

Fig. 8. A visual representation of the most-likely wave spectrum for the third rogue wave threshold $H_{rogue} \geq 18.26$ m.

Note that only the H_{rogue}, and not the η_{rogue}, thresholds from Table 2 are used to generate these rogue time series. However, considering that the return-periods for exceeding the η_{rogue} thresholds are significantly longer than the H_{rogue} return-periods in the same sea states, the H_{rogue}-defined rogue time series present indeed a more 'most-likely' scenario, and one more relevant for the design lifetime of such an offshore structure. In addition, the H_{rogue} definitions allow for a more direct comparison, versus the η_{rogue} thresholds where the preceding wave crest or trough magnitude may vary significantly based on the underlying wave spectrum.

Fig. 9 gives an example of a most-likely autocorrelation function used to generate the rogue wave deterministic shape, based on the third rogue wave threshold $H_{rogue} \geq 18.26$ m, where the considered spectra are the those from Fig. 8. For each size rogue wave, five random wave time histories are generated with a deterministic rogue wave at 350 s and a total length of 462 s. In these five simulations, the deterministic

Table 7
Parameters of the wind turbine and spar substructure.

5 MW wind turbine		OC3-Hywind spar substructure	
Parameter	Value	Parameter	Value
Rotor, hub diameter	126 m, 3 m	Total draft	120 m
Hub height	90 m	Elevation to platform top above SWL	10 m
Cut-in, rated, cut-out wind speed	3 m/s, 14 m/s, 25 m/s	Depth to top of taper below SWL	4 m
Rotor mass	110,000 kg	Depth to bottom of taper below SWL	12 m
Nacelle mass	240,000 kg	Platform diameter above taper	6.5 m
Nacelle dimension (l × b × h)	14.285 × 2.286 × 3.500 m	Platform diameter below taper	9.4 m
Nacelle drag areas (x, y, z)	$8.0, 50.0, 32.7\ m^2$	Total platform mass	7,466,330 kg
Nacelle inertia (about x, y, z axis)	350020, 5409970, 2607890 kgm^2	Number of mooring lines	3
Drag coefficient (C_D) (along x, y, z)	1.0, 1.2, 1.2	Depth to fairleads below SWL	70 m
Tower mass	347,460 kg	Depth to anchors below SWL	320 m
Coordinate center of mass	(0.2 m, 0.0 m, 64 m)		

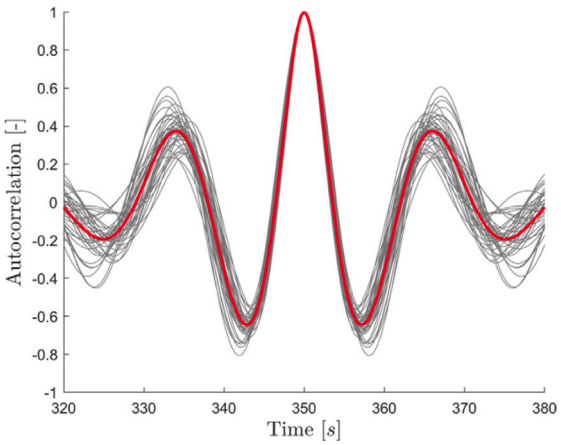

Fig. 9. A visual representation of the most-likely rogue wave shape for the third rogue wave threshold $H_{rogue} \geq 18.26$ m.

rogue wave shape based on the NewWave formulation remains constant while the stochastic wave time series is determined by a different seed, as directed by the most-likely wave model (Taylor et al., 1997).

5.2. Dynamic response

The dynamic analysis software OrcaFlex was used to evaluate the dynamic response of the open-source OC3-Hywind concept model (Orcina, 2019). The OC3-Hywind incorporates a spar substructure based on the Equinor Hywind Scotland SFWT with a 5MW NREL reference turbine, an industry-standard reference model representative for a utility-scale, multi-megawatt wind turbine (Jonkman et al., 2009). To keep the turbine from drifting, the spar is anchored to the sea bed by three catenary mooring lines. The spar has a draft of 120 m and the top, upon which the turbine tower is placed, extends 10 m above the still water line (SWL).

5.2.1. System modeling

The OC3-Hywind concept model has parameters as given in Table 7 and is built up out of the following components: the turbine, the tower, the spar platform and the mooring system. The turbine element is a conventional three-bladed rotor, with options for variable speed and pitch control. A gear ratio can be specified and is set to 97 for the OC3-Hywind model. The rotor hub has a radius of 1.5 m and is assigned to the turbine object. The transverse and axial moments of inertia around the main shaft are specified and the center of mass of the hub is located at the geometric center of the rotor.

The turbine blades in OrcaFlex are modeled by a structural model somewhat similar to the one used by lines, with inertia lumped at the nodes which are connected by massless segments. Each blade consists of 17 different elements, which can vary in length, wing type and (initial) pitch angle. The blade DOFs are set to free, which means that for each node, 6 DOFs are included. This allows the blade parts to move in a rotational and translational direction with respect to each other, thus allowing the blade flexibility to be modeled. The nacelle is modeled as a lumped 6-DOF buoy object, with the proper mass, center of mass, and inertial properties. To account for the aerodynamic effects, a massless drag line with appropriate drag and added mass coefficients is further attached to the nacelle, as in OrcaFlex aerodynamic effects cannot be captured for the 6-DOF buoy object on its own (Orcina, 2019).

The conical tower is modeled as a line object with a 'homogeneos pipe' line type assigned to it. By doing so, a variable wall thickness can be modeled with the appropriate inner and outer diameters, as well as the physical properties of the tower such as the material density, Young's modulus and Poisson ratio. This leads to a model where OrcaFlex can take the structural deflection of the tower into account.

The spar platform is modeled in Orcaflex using the 'spar' category of the 6D buoy element. This results in a rigid body spar platform, with 6 DOFs and the appropriate geometric and physical properties assigned to it. The spar buoy is split up into 40 discrete cylinders. To accurately capture changes to the hydrodynamic loading and buoyancy on the surface-piercing part of the spar buoy, the cylindric parts in the top section have been assigned a fine discretization of 1 m, while for the lower part a discretization of 10 m is considered (see Fig. 10). To calculate the hydrodynamic loads on the spar in Orcaflex, the Morison equation extended for a moving body is considered (Eq. (8)). The influence of radiation damping and diffraction effects are assumed negligible, as is assumed by the OC3 NREL report (Jonkman, 2010).

$$F = \Delta a_f + C_a \Delta a_r + \frac{1}{2}\rho C_D A |v_r| v_r \tag{8}$$

where

f = fluid force
Δ = fluid mass displaced by the body
a_f = fluid acceleration relative to earth
C_a = body added mass coefficient
a_r = fluid acceleration relative to the body
ρ = water density
v_r = fluid velocity relative to the body
C_D = body drag coefficient
A = drag area

The three catenary mooring lines holding the spar in place are assigned their physical properties via the appropriate line type elements. The anchors and mooring lines are placed evenly around the spar in azimuth increments of 120°, and the radius of the anchors to the centerline of the spar is approximately 854 m. The mooring lines are connected to the spar via a 'delta' or 'crowfoot' connection, as illustrated in Fig. 11. Each line is connected to the spar at a

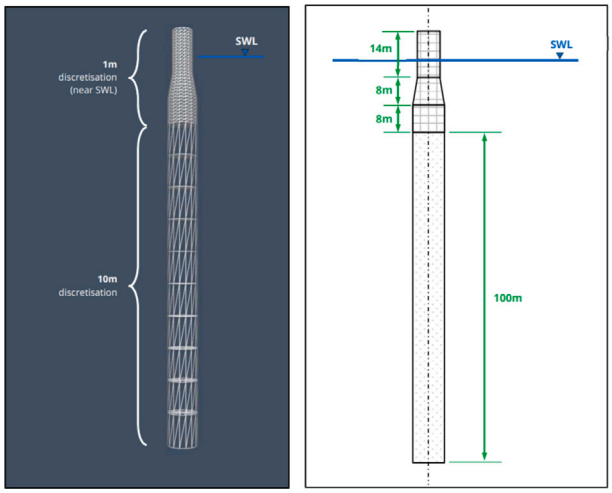

Fig. 10. The OC3-Hywind spar substructure as built in OrcaFlex.
Source: Retrieved from Ross and McKinnon (2018).

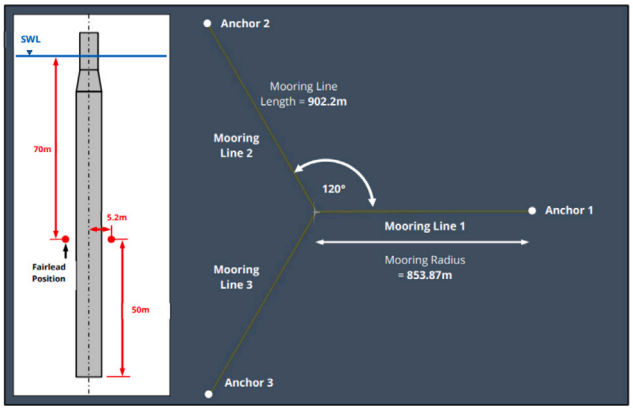

Fig. 11. The mooring line arrangement of the OrcaFlex OC3-Hywind model.
Source: Retrieved from Ross and McKinnon (2018).

radius of 5.2 m measured from the spar's centerline. The mooring lines were modeled in OrcaFlex by the analytic catenary method, which considers line properties like weight, buoyancy, axial stiffness, and axial seabed friction but ignores bend stiffness, drag, and added mass. Within OrcaFlex simulations, lookup tables are used to relate the mooring line fairlead tension to some offset value. Note that such large rogue waves could also lead to slack-line events in the mooring lines, see, e.g. Robertson et al. (2017), though such an effect has not been examined for the simple application considered here.

During the simulations, only the wave loads are considered. The wind and current speeds are set to 0 m/s, and the turbine is assumed to be in a parked condition. The dynamic response of the SFWT to the rogue wave was investigated on the basis of the surge, heave, pitch and nacelle acceleration. Table 8 presents the results of five simulations. For each parameter, the average maximum of the five simulations is reported, which were found directly or shortly after the rogue wave impact.

Some observations regarding the results from Table 8:

- The largest rogue wave led to the largest surge response of 16.91 m, followed by the third largest rogue wave inducing a surge response of 15.32 m.
- The heave response is mild overall. The largest rogue wave led to the largest response, which was only 3.02 m. This comes as no surprise, as spar designs are designed to reduce heave motions (Ma and Patel, 2001).

Table 8
Dynamic response results from the five OrcaFlex rogue wave simulations for each embedded rogue wave height and corresponding crest height. Reported values are the average of the maximums of five simulations. Surge, heave and pitch are evaluated for the spar at the height of the mean sea level, MSL.

Rogue wave threshold [m]	Average rogue crest height [m]	Surge [m]	Heave [m]	Pitch [°]	Nacelle acceleration [m/s^2]
H_{rogue} = 20.62 m	11.25	16.91	3.02	7.15	3.81
H_{rogue} = 19.84 m	11.20	14.31	2.51	6.35	3.83
H_{rogue} = 18.26 m	10.05	15.32	2.53	6.97	3.82
H_{rogue} = 17.56 m	9.95	13.07	2.01	5.63	3.69

- The largest rogue wave led to the largest pitch angle of 7.15°, followed by the third largest rogue wave inducing a pitch angle of 6.97°.
- The top three rogue wave sizes produced almost identical averaged nacelle accelerations of about 3.81–3.83 m/s^2, and the response to the fourth rogue wave is very close to this value.

Simulations with a larger rogue wave do not always induce motions which are much more extreme than the smaller waves. The random seeds used to generate the underlying wave spectrum are different for each simulation, which leads to more or less favorable initial conditions of the floating turbine system before the rogue wave impact. Due to this, some lower rogue waves may induce similar or more extreme motions than the larger ones.

It is difficult to make unambiguous conclusions regarding the potential danger of a rogue wave to the SFWT based only on the dynamic response. There are no specific limits for translational displacements of a catenary moored SFWT. Mostly the pitch angles and nacelle accelerations are limiting, due to stability criteria and the presence of sensitive components in the nacelle. In the industry, these maximum angles and accelerations of wind turbines are imposed by the turbine original equipment manufacturers and are treated secretively.

In the literature, a few claims have been made regarding maximum allowable inclination and nacelle accelerations. Papers that discuss the pitch angle state that the maximum pitch angle should be taken as 10° (see, *e.g.*, Sclavounos et al. (2008), Huijs et al. (2013), Kolios et al. (2015), Taboada et al. (2020)). In absence of exact values from the industry, 10° may be used as a reference value. Regarding the nacelle acceleration, some papers state that 0.4 g (3.92 m/s^2) is a common industry limit (Boo et al., 2013, 2017; Taboada et al., 2020). Other papers assume lower limits, such as 0.3 g (Nejad and Torsvik, 2021), or even 0.2 g (Leimeister, 2017). When comparing the responses of Table 8 with the reference values found in the literature, the rogue-induced pitch angles are below the conventional literature limit of 10° and the nacelle accelerations are below 0.4 g. However, the nacelle accelerations can be said to be significant, as they are only slightly below the 0.4 g literature limit, and notably higher than the lower 0.2 g and 0.3 g limits.

Since the reference values are not exceeded and the return periods (Table 5) for the four rogue waves indicate that these waves can be considered a once-in-a-lifetime event for a typical offshore structure, where the most conservative statistical model estimates return periods of over 100 years for the two largest rogue waves, it appears that these rogue waves alone present no danger to the spar-type floating wind turbine.

6. Conclusions

In this paper, the occurrence probability of several rogue waves was investigated using statistical wave models and a significant amount of historical wave data. Two rogue wave size definitions, one regarding the wave crest, and the other regarding the crest-to-trough height, were evaluated separately using two statistical approaches. The first approach estimates a wave height at a point in time by time-extreme models (the Forristall (2000), Tayfun (1980), Tayfun and

Fedele (2007), Naess (1985), and Rayleigh (Longuet-Higgins, 1952) model). The second approach estimates the wave height over an area in time via space–time extreme models (the STE2 model from Benetazzo et al. (2015) and STE1QD model from Boccotti (2000)).

The area size which leads to the STE models estimating a higher rogue wave occurrence probability than the TE models was investigated. Four rogue crest and wave heights were established using the highest measured sea states and for these waves the return periods until a 95% occurrence probability were calculated. The area size for which the STE models were evaluated was based on the OC3-Hywind spar diameter, for which an application of the probabilistic rogue wave analysis was presented. The dynamic response of the OC3-Hywind spar to the four considered rogue waves was evaluated in Orcaflex. Using both the dynamic response and the long-term occurrence probability of the rogue wave, this research presents a new and advanced approach for a risk analysis of rogue waves to offshore structures.

The main findings of this study can be summarized as follows:

- For the TE wave crest models it was observed that the Forristall model estimates the lowest rogue crest occurrence probabilities, followed by the Tayfun model. The Tayfun–Fedele model estimates the highest probabilities. Of those three models, only the Tayfun–Fedele model estimates higher probabilities than the STE2 model from Benetazzo et al. in two sea states, for an area size smaller than 2×2 m^2. When the occurrence probability of rogue crests is considered on a spatial scale relevant for (floating) offshore wind turbines, incorporating the spatial dimension using the STE2 model will result in the most conservative estimate.
- Regarding the crest-to-trough models, it was observed that the STE1QD model from Boccotti estimates higher exceedance probabilities of the rogue threshold than the Naess model for all areas in all sea states. The Rayleigh model estimates higher probabilities than the STE1QD model in several sea states for an area size smaller than 12×12 m^2. When the area size was smaller than 2×2 m^2, the Rayleigh model estimated higher probabilities in all sea states. While evaluating the long term rogue wave occurrence probability, it was observed that for the considered area of 6.5×6.5 m^2 the STE1QD model already became more conservative than the Rayleigh model.
- The dynamic response of the OC3-Hywind spar to the four rogue waves did not exceed the maximum reference values, but they can be considered quite serious as some did exceed lower thresholds. Based on the fact that for the two largest rogue waves the most conservative probability model estimates a return period of over 100 years until a 95% occurrence probability, and all four waves induced a dynamic response which did not exceed maximum reference limits, it appears that effects from these rogue waves alone present no obvious danger for the considered SFWT. However, ultimately this will depend on the sensitivity of the components inside the turbine, the included effects of wind and current, as well as the desired risk profile of the wind farm owner.

Future work can be imagined for both the probabilistic rogue wave estimations and the resulting spar dynamic modeling. For the former topic, many interesting questions arise when considering what would be the effect of looking at different locations or potentially even more buoy data. This analysis did not explicitly compare the rogue probabilistic models based on the wave spreading, which could also have interesting effects. For the latter topic, more simulations could be used for a more in-depth risk analysis, considering also rogue waves defined by longer return-periods. In addition, some other effects, such as slack-line events in the mooring lines, have been mentioned as other factors to consider for examining the effects of rogue wave impacts on spar-type floating wind turbines.

CRediT authorship contribution statement

T.P. Nederkoorn: Data analysis. **H.C. Seyffert:** Supervised, Aided in writing the manuscript.

Declaration of competing interest

The authors declare that they have no known competing financial interests or personal relationships that could have appeared to influence the work reported in this paper.

Acknowledgments

The authors would like to thank Dr. Ping Liu at INTECSEA and Dr. Carey Walters at TU Delft for sharing their insightful guidance and curiosity, which strongly improved the research carried out for this paper. The authors further thank the anonymous reviewers for their thorough and thoughtful reviews.

Appendix. Statistical wave models

This appendix describes the considered statistical wave models used in this study. The TE and STE models are considered separately for the wave crest or crest-to-trough models.

A.1. Crest-to-trough heights - Time extreme

The Rayleigh distribution is generally said to overestimate wave heights occurring at a certain location. A better estimation is given by a bandwidth-corrected version of the Rayleigh distribution, originally presented by Naess (1985):

$$P_N\left(H > z\right) = \exp\left[-\frac{4}{1-\Psi^*}\left(\frac{z}{H_s}\right)^2\right] \tag{A.1}$$

This distribution accounts for finite-bandwidth effects by incorporating the bandwidth parameter ψ^*. Here ψ^* is the minimum of the autocorrelation function of the sea surface $\psi(t)$, which can be estimated from the wave spectrum as:

$$\psi(t) = \frac{1}{\sigma^2}\iint S(\omega,\theta)d\theta\cos(\omega t)d\omega \tag{A.2}$$

The Rayleigh distribution of wave heights from Longuet-Higgins (1952) is recovered from Eq. (A.1) when $\psi^* = -1$:

$$P_{Rh}\left(H > z\right) = \exp\left[-2\left(\frac{z}{H_s}\right)^2\right] \tag{A.3}$$

A.2. Crest heights - Time extreme

The Tayfun distribution approximates second-order Stokes' waves (Tayfun, 1980). It is sometimes called a Rayleigh–Stokes distribution (Nerzic and Prevosto, 1998) because it describes crest heights by a first-order Gaussian process (therefore having a Rayleigh crest distribution, Eq. (A.4)) with a second-order Stokes expansion. The Tayfun distribution is solely dependent on a dimensionless wave steepness parameter μ, and is given by Eq. (A.5). (see, *e.g.,* Tayfun and Fedele (2007))

$$P_{Rc}\left(\eta_c/\sigma > z\right) = \exp\left[-\frac{z^2}{2}\right] \tag{A.4}$$

$$P_{\mathrm{T}}\left(\eta_c/\sigma > \xi\right) = \exp\left[-\frac{1}{2}\left(\frac{-1+\sqrt{1+2\mu\xi}}{\mu^2}\right)^2\right] \tag{A.5}$$

where $\xi = z(1+\mu z/2)$ is the second-order wave envelope related to the first-order wave envelope z which follows the Rayleigh distribution, and μ is a wave steepness parameter:

$$\mu = \mu_m\left(1-\nu+\nu^2\right) \tag{A.6}$$

where

$$\mu_m = \sigma \left(2\pi m_{001}/m_{000}\right)^2 / g \tag{A.7}$$

is corrected with the spectral bandwidth, Eq. (A.9) (Fedele and Tayfun, 2009) and the directional moments m_{ijk} are calculated by Eq. (5).

$$\varepsilon = \sqrt{1 - \frac{m_2^2}{m_0 m_4}} \tag{A.8}$$

$$\nu = \sqrt{\frac{m_2 m_0}{m_1 m_1}} - 1 \tag{A.9}$$

The Forristall model, Eq. (A.10), is based on the Weibull distribution fitted to second order simulations and experimental data (Forristall, 2000).

$$P_{\mathrm{F}}\left(\eta_c > z\right) = \exp\left[-\left(\frac{z}{\alpha H_s}\right)^{\beta}\right] \tag{A.10}$$

The parameters α and β are found as functions of the wave spectrum and the water depth. These are based on the degree of nonlinearity as given by the wave steepness and the Ursell number. The steepness number used in the fits is given by:

$$S_1 = \frac{2\pi}{g}\frac{H_s}{T_1^2} \tag{A.11}$$

where $T_1 = m_0/m_1$ is the spectral mean wave period. Here, the Ursell number is given by:

$$\mathrm{Ur} = \frac{H_s}{k_1^2 d^3} \tag{A.12}$$

where k_1 is the wave number for the frequency $1/T_1$. The fits of the parameters α and β to the 3D wave data can then be written as:

$$\alpha = 0.3536 + 0.2568 S_1 + 0.0800\mathrm{Ur} \tag{A.13}$$

$$\beta = 2 - 1.7912 S_1 - 0.5302\mathrm{Ur} + 0.284\mathrm{Ur}^2 \tag{A.14}$$

The Tayfun–Fedele model is an improvement of the Tayfun model to include third-order nonlinearities (Tayfun and Fedele, 2007). The probability of exceedance of a normalized crest by the Tayfun–Fedele model is given by:

$$P_{\mathrm{TF}}\left(\eta_c/\sigma > \xi\right) = \exp\left[-\frac{1}{2}\left(\frac{-1+\sqrt{1+2\mu\xi}}{\mu^2}\right)^2\right] \times \left[1 + \frac{\Lambda}{64}\xi^2\left(\xi^2 - 4\right)\right] \tag{A.15}$$

where μ again is the wave steepness as presented in Eq. (A.6), $\xi = z(1 + \mu z/2)$, and Λ is a function of the joint fourth-order cumulants of the surface elevation. Λ may in practice be approximated only as a function of the excess kurtosis by $\Lambda_{\mathrm{appr}} = 8\lambda_{40}/3$, where in deep water the bound component reduces to the simple form $\lambda_{40}^b = 18\mu_m$ (Fedele et al., 2016).

A.3. Crest heights — Space–time extreme

The STE1 model from Fedele considers a stationary homogeneous Gaussian wave field $\eta(x, y, t)$ which is bounded by a space–time volume $V_{st} = XYD$, where X and Y are the spatial dimensions and D represents some duration of time (Fedele, 2012). The model considers the average number of waves within the 3D domain N_V, waves on the 2D surfaces N_S along the 1D perimeter N_B of the considered spatial domain.

$$N_B = \frac{X}{L_x} + \frac{Y}{L_y} + \frac{D}{T_m} \tag{A.16}$$

$$N_S = \sqrt{2\pi}\left(\frac{XD}{L_x T_m}\sqrt{1-\alpha_{xt}^2} + \frac{XY}{L_x L_y}\sqrt{1-\alpha_{xy}^2} + \frac{YD}{L_y T_m}\sqrt{1-\alpha_{yt}^2}\right) \tag{A.17}$$

$$N_V = 2\pi\frac{XYD}{L_x L_y T_m}\sqrt{1-\alpha_{xt}^2-\alpha_{xy}^2-\alpha_{yt}^2+2\alpha_{xt}\alpha_{xy}\alpha_{yt}} \tag{A.18}$$

Here, T_m is the mean zero-crossing period, L_x and L_y are the mean components of the wavelength in $x-$ and $y-$direction, and α_{xt}, α_{yt} and α_{xy} are the irregularity parameters of the sea state. These irregularity parameters account for correlations between space and time or space and space so that waves are not counted twice. All these parameters are given by Eq. (A.19)–(A.24):

$$T_m = \sqrt{\frac{m_{000}}{m_{002}}} \tag{A.19}$$

$$L_x = 2\pi\sqrt{\frac{m_{000}}{m_{200}}} \tag{A.20}$$

$$L_y = 2\pi\sqrt{\frac{m_{000}}{m_{020}}} \tag{A.21}$$

$$\alpha_{xt} = \frac{m_{101}}{\sqrt{m_{200}m_{002}}} \tag{A.22}$$

$$\alpha_{yt} = \frac{m_{011}}{\sqrt{m_{020}m_{002}}} \tag{A.23}$$

$$\alpha_{xy} = \frac{m_{110}}{\sqrt{m_{200}m_{020}}} \tag{A.24}$$

Now, the exceedance probabilities that a 3D crest height normalized by σ exceeds a certain threshold z within the 3D volume, on the 2D surfaces, and along the 1D perimeter are given by:

$$P_B\left\{\eta_c/\sigma > z \mid B\right\} = P_{\mathrm{Rc}} \tag{A.25a}$$

$$P_S\left\{\eta_c/\sigma > z \mid S\right\} = zP_{\mathrm{Rc}} \tag{A.25b}$$

$$P_V\left\{\eta_c/\sigma > z \mid V\right\} = \left(z^2 - 1\right)P_{\mathrm{Rc}} \tag{A.25c}$$

with P_{Rc} representing the Rayleigh wave crest distribution from Eq. (A.4). The probability the global surface maximum η_{max} exceeds threshold z (given $z \gg 1$) over the 3D volume by the space–time model (STE1) is given by Eq. (A.26).

$$\begin{aligned} &P_{\mathrm{STE1,max}}\left\{\eta_{\max}/\sigma > z \mid \left(N_V, N_S, N_B\right)\right\} \\ &\approx \left[1-\left(1-P_V\right)^{N_V}\right] + \left[1-\left(1-P_S\right)^{N_S}\right] + \left[1-\left(1-P_B\right)^{N_B}\right] \\ &\approx N_V P_V + N_S P_S + N_B P_B \approx \left(N_V z^2 + N_S z + N_B\right)P_{\mathrm{Rc}} \end{aligned} \tag{A.26}$$

Benetazzo et al. extended the STE1 model to include the second-order contribution of the waves ξ, as originally presented in the Tayfun model, here called the STE2 model (Benetazzo et al., 2015):

$$P_{\mathrm{STE2,max}}\left\{\eta_{\max}/\sigma > \xi \mid \left(N_V, N_S, N_B\right)\right\} \approx \left(N_V z^2 + N_S z + N_B\right)P_{\mathrm{Rc}} \tag{A.27}$$

The Gumbell asymptotic limit ensures exceedance probabilities smaller than 1 for small thresholds, resulting in Eqs. (A.30) and (A.31) in Box I for the STE1 and STE2 models, respectively. Here h_{st} is the dimensionless most probable extreme value η_{max}/σ which can be found by solving the following implicit equation:

$$\left(N_V h_{st}^2 + N_S h_{st} + N_B\right)\exp\left(-h_{st}^2/2\right) = 1 \tag{A.28}$$

$$P_{\mathrm{STE1,max}}\left\{\eta_{\max}/\sigma > z \mid \left(N_V, N_S, N_B\right)\right\} \approx \exp\left\{-\exp\left[-\left(z - h_{\mathrm{ST}}\right)\left(h_{\mathrm{ST}} - \frac{2N_V h_{\mathrm{ST}} + N_S}{N_V h_{\mathrm{ST}}^2 + N_S h_{\mathrm{ST}} + N_B}\right)\right]\right\} \tag{A.30}$$

$$P_{\mathrm{STE2,max}}\left\{\eta_{\max}/\sigma > \xi \mid \left(N_V, N_S, N_B\right)\right\} \approx \exp\left\{-\exp\left[-\frac{\left(\xi - h_{\mathrm{ST}} - \frac{\mu}{2}h_{\mathrm{ST}}^2\right)\left(h_{\mathrm{ST}} - \frac{2N_V h_{\mathrm{ST}}+N_S}{N_V h_{\mathrm{ST}}^2+N_S h_{\mathrm{ST}}+N_B}\right)}{1+\mu h_{\mathrm{ST}}}\right]\right\} \tag{A.31}$$

$$P_{\mathrm{STE1QD,max}}\left\{H_{max} > H \mid \left(N_V, N_S, N_B\right)\right\} \approx \exp\left\{-\exp\left[-\left(H - h_{\mathrm{ST}}\cdot\sigma\sqrt{2(1-\psi^*)}\right)\left(\frac{h_{\mathrm{ST}} - \frac{2N_V h_{\mathrm{ST}}+N_S}{N_V h_{\mathrm{ST}}^2+N_S h_{\mathrm{ST}}+N_B}}{\sigma\sqrt{2(1-\psi^*)}}\right)\right]\right\} \tag{A.32}$$

Box I.

A.4. Crest-to-trough heights — Space–time extreme

By extending the linear STE1 model, an expression can be formulated for a space–time crest-to-trough model. For this purpose, use is made of the Quasi-Determinism theory presented by Boccotti (2000). This linear theory states that the largest waves in a certain sea state follow a deterministic shape, based on the autocorrelation function of the wave spectrum as earlier defined by Eq. (A.2). Using the deterministic shape of the largest waves, the relation between crest and crest-to-trough height can be estimated as:

$$H = \sqrt{2(1-\psi^*)}\cdot\eta \tag{A.29}$$

Again ψ^* is defined as the minimum of the autocorrelation function based on Eq. (A.2). Rewriting Eq. (A.30) using the deterministic relationship of crest and crest-to-trough yields Eq. (A.32) for the STE1QD model (Boccotti, 2000) (see Eqs. (A.30)–(A.32) in Box I).

References

Adcock, T.A.A., Taylor, P.H., Yan, S., Ma, Q.W., Janssen, P.A.E.M., 2011. Did the Draupner wave occur in a crossing sea? Proc. R. Soc. A 467 (2134), 3004–3021.

Adler, Robert J., Taylor, Jonathan E., 2009. Random Fields and Geometry. Springer Science & Business Media.

Barbariol, Francesco, Bidlot, Jean-Raymond, Cavaleri, Luigi, Sclavo, Mauro, Thomson, Jim, Benetazzo, Alvise, 2019. Maximum wave heights from global model reanalysis. Prog. Oceanogr. (ISSN: 0079-6611) 175, 139–160. http://dx.doi.org/10.1016/j.pocean.2019.03.009.

Benetazzo, Alvise, Ardhuin, Fabrice, Bergamasco, Filippo, Cavaleri, Luigi, Guimaraes, Pedro Veras, Schwendeman, Michael, Sclavo, Mauro, Thomson, Jim, Torsello, Andrea, 2017. On the shape and likelihood of oceanic rogue waves. Sci. Rep. 7 (1), 1–11.

Benetazzo, Alvise, Barbariol, Francesco, Bergamasco, Filippo, Torsello, Andrea, Carniel, Sandro, Sclavo, Mauro, 2015. Observation of extreme sea waves in a space–time ensemble. J. Phys. Oceanogr. 45 (9), 2261–2275.

Benetazzo, Alvise, Barbariol, Francesco, Davison, Silvio, 2020. Short-term/range extreme-value probability distributions of upper bounded space-time maximum ocean waves. J. Mar. Sci. Eng. 8 (9), 679.

Boccotti, Paolo, 2000. Wave Mechanics for Ocean Engineering. Elsevier.

Boo, Sung Youn, Shelly, Steffen Allan, Kim, Daejun, 2017. Design and dynamic performances of Y-wind floating offshore wind turbine platform. In: The 27th International Ocean and Polar Engineering Conference. International Society of Offshore and Polar Engineers.

Boo, Sung, Zou, Jun, Im, S.W., 2013. Conceptual design of 5MW floating wind turbines for Korean offshore. In: The 2013 World Congress on Advances in Structural Engineering and Mechanics, Jeju, Korean.

Casas-Prat, Mercè, Holthuijsen, Leo H., 2010. Short-term statistics of waves observed in deep water. J. Geophys. Res. Oceans 115 (C9).

Cattrell, A.D., Srokosz, M., Moat, B.I., Marsh, R., 2018. Can rogue waves be predicted using characteristic wave parameters? J. Geophys. Res. Oceans 123 (8), 5624–5636.

Cattrell, A.D., Srokosz, M., Moat, B.I., Marsh, R., 2019. Seasonal intensification and trends of rogue wave events on the US western seaboard. Sci. Rep. 9 (1), 4461. http://dx.doi.org/10.1038/s41598-019-41099-z.

Cavaleri, Luigi, Barbariol, Francesco, Benetazzo, Alvise, Bertotti, Luciana, Bidlot, Jean-Raymond, Janssen, Peter, Wedi, Nils, 2016. The Draupner wave: A fresh look and the emerging view. J. Geophys. Res. Oceans 121 (8), 6061–6075.

Cavaleri, L., Bertotti, L., Torrisi, L., Bitner-Gregersen, E., Serio, M., Onorato, M., 2012. Rogue waves in crossing seas: The Louis Majesty accident. J. Geophys. Res. Oceans 117 (C11).

Christou, Marios, Ewans, Kevin, 2011a. Examining a comprehensive dataset containing thousands of freak wave events: Part 1—Description of the data and quality control procedure. In: International Conference on Offshore Mechanics and Arctic Engineering. pp. 815–826. http://dx.doi.org/10.1115/OMAE2011-50168.

Christou, Marios, Ewans, Kevin, 2011b. Examining a comprehensive dataset containing thousands of freak wave events: Part 2—Analysis and findings. In: International Conference on Offshore Mechanics and Arctic Engineering. pp. 827–837. http://dx.doi.org/10.1115/OMAE2011-50169.

Christou, Marios, Ewans, Kevin, 2014. Field measurements of rogue water waves. J. Phys. Oceanogr. 44 (9), 2317–2335.

2017. Environmental Loads Recommended Practice DNV-RP-C205. Technical report, DNV.

Dysthe, Kristian, Krogstad, Harald E., Müller, Peter, 2008. Oceanic rogue waves. Annu. Rev. Fluid Mech. (ISSN: 00664189) 40, 287–310.

Earle, M.D., Steele, K.E., Wang, D.W.C., 1999. Use of advanced directional wave spectra analysis methods. Ocean Eng. 26 (12), 1421–1434.

Ersdal, Gerhard, Hörnlund, Erik, 2008. Assessment of offshore structures for life extension. In: International Conference on Offshore Mechanics and Arctic Engineering. pp. 277–284.

Fedele, Francesco, 2012. Space–time extremes in short-crested storm seas. J. Phys. Oceanogr. 42 (9), 1601–1615.

Fedele, Francesco, Brennan, Joseph, De León, Sonia Ponce, Dudley, John, Dias, Frédéric, 2016. Real world ocean rogue waves explained without the modulational instability. Sci. Rep. 6, 27715.

Fedele, Francesco, Tayfun, M. Aziz, 2009. On nonlinear wave groups and crest statistics. J. Fluid Mech. 620, 221.

Forristall, George Z., 2000. Wave crest distributions: Observations and second-order theory. J. Phys. Oceanogr. 30 (8), 1931–1943.

Google maps, 2021. Satellite image Monterey Bay.

Gorman, Richard, 2018. Estimation of directional spectra from wave buoys for model validation. Procedia IUTAM 26, 81–91. http://dx.doi.org/10.1016/j.piutam.2018.03.008.

Häfner, Dion, Gemmrich, Johannes, Jochum, Markus, 2021. Real-world rogue wave probabilities. Sci. Rep. 11 (1), 10084. http://dx.doi.org/10.1038/s41598-021-89359-1.

Haver, Sverre, 2001. Evidences of the existence of freak waves. In: Rogue Waves. pp. 129–140.

Holthuijsen, Leo H., 2007. Waves in Oceanic and Coastal Waters. Cambridge University Press, http://dx.doi.org/10.1017/CBO9780511618536.

Huijs, Fons, Mikx, Joop, Savenije, Feike, de Ridder, Erik-Jan, 2013. Integrated design of floater, mooring and control system for a semi-submersible floating wind turbine. In: Proceedings of the EWEA Offshore, Frankfurt, Germany, Vol. 19. p. 21.

Jonkman, Jason, 2010. Definition of the Floating System for Phase IV of OC3. Technical report, National Renewable Energy Lab (NREL), Golden, CO (United States).

Jonkman, Jason, Butterfield, Sandy, Musial, Walter, Scott, George, 2009. Definition of a 5-MW Reference Wind Turbine for Offshore System Development. Technical report, National Renewable Energy Lab.(NREL), Golden, CO (United States).

Karmpadakis, I., Swan, C., Christou, M., 2019. Laboratory investigation of crest height statistics in intermediate water depths. Proc. R. Soc. Lond. Ser. A Math. Phys. Eng. Sci. 475 (2229), 20190183.

Kolios, A., Borg, M., Hanak, D., 2015. Reliability analysis of complex limit states of floating wind turbines. J. Energy Chall. Mech. 2 (1), 6–9.

Krogstad, Harald E., Liu, Jingdong, Socquet-Juglard, Herve, Dysthe, Kristian B., Trulsen, Karsten, 2004. Spatial extreme value analysis of nonlinear simulations of random surface waves. In: International Conference on Offshore Mechanics and Arctic Engineering. pp. 285–295.

Latheef, M., Swan, C., 2013. A laboratory study of wave crest statistics and the role of directional spreading. Proc. R. Soc. A 469 (20120696), http://dx.doi.org/10.1098/rspa.2012.0696.

Leimeister, Mareike, 2017. Global limit states for the design of floating wind turbine support structures. In: 13th EAWE PhD Seminar.

Longuet-Higgins, Michael S., 1952. On the statistical distribution of the heights of sea waves. J. Mar. Res. 11 (3), 245–266.

Longuet-Higgins, Michael S., 1961. Observations of the directional spectrum of sea waves using the motions of a floating buoy. Ocean Wave Spectra.

Ma, Q.W., Patel, M.H., 2001. On the non-linear forces acting on a floating spar platform in ocean waves. Appl. Ocean Res. 23 (1), 29–40.

McAllister, M.L., van den Bremer, T.S., 2020. Experimental study of the statistical properties of directionally spread ocean waves measured by buoys. J. Phys. Oceanogr. 50 (2), 399–414.

Mori, Nobuhito, 2003. Effects of wave breaking on wave statistics for deep-water random wave train. Ocean Eng. (ISSN: 0029-8018) 30 (2), 205–220. http://dx.doi.org/10.1016/S0029-8018(02)00017-3.

Mori, Nobuhito, Janssen, Peter A.E.M., 2006. On kurtosis and occurrence probability of freak waves. J. Phys. Oceanogr. 36 (7), 1471–1483.

Naess, Arvid, 1985. On the distribution of crest to trough wave heights. Ocean Eng. 12 (3), 221–234.

Nejad, Amir R., Torsvik, Jone, 2021. Drivetrains on floating offshore wind turbines: lessons learned over the last 10 years. Forsch. Ing. 1–9.

Nerzic, Raymond, Prevosto, Marc, 1998. A Weibull-Stokes model for the distribution of maximum wave and crest heights. Int. J. Offshore Polar Eng. 8, 2.

Orcina, 2019. K01 Floating wind turbine Orcaflex model. URL https://www.orcina.com/resources/examples/?key=k.

Qu, Xiaoqi, Li, Yan, Tang, Yougang, Hu, Zhiqiang, Zhang, Pei, Yin, Tianchang, 2020. Dynamic response of spar-type floating offshore wind turbine in freak wave considering the wave-current interaction effect. Appl. Ocean Res. 100, 102178.

Robertson, A., Wendt, F., Jonkman, J., Popko, W., Dagher, H., Gueydon, S., Qvist, J., Vittori, F., Azcona, J., Uzunoglu, E., Soares, C., Harries, R., Yde, A., Galinos, C., Hermans, K., De Vaal, J., Bozonnet, P., Bouy, L., Bayati, I., Bergua, R., Galvan, J., Mendikoa, I., Sanchez, C., Shin, H., Oh, S., Molins, C., Debruyne, Y., 2017. OC5 project phase II: Validation of global loads of the DeepCwind floating semisubmersible wind turbine. Energy Procedia 38–57.

Rosenthal, W., Lehner, S., 2008. Rogue waves: Results of the MaxWave project. J. Offshore Mech. Arct. Eng. (ISSN: 0892-7219) 130 (2), http://dx.doi.org/10.1115/1.2918126, 021006.

Ross, A., McKinnon, G., 2018. Orcina Project 1405 Wind Turbine Validation Report. Technical report, Orcina.

Ruzzo, Carlo, Arena, Felice, 2019. A numerical study on the dynamic response of a floating spar platform in extreme waves. J. Mar. Sci. Technol. 24 (4), 1135–1152.

Schubert, Matthias, Wu, Yanyun, Tychsen, Jesper, Dixen, Martin, Faber, Michael Havbro, Sørensen, John Dalsgaard, Jonathan, Philip, 2020. On the distribution of maximum crest and wave height at intermediate water depths. Ocean Eng. (ISSN: 0029-8018) 217, 107485. http://dx.doi.org/10.1016/j.oceaneng.2020.107485.

Sclavounos, Paul, Tracy, Christopher, Lee, Sungho, 2008. Floating offshore wind turbines: Responses in a seastate pareto optimal designs and economic assessment. In: International Conference on Offshore Mechanics and Arctic Engineering, Vol. 48234. pp. 31–41.

Taboada, Miguel, Ortega, Alvaro, Martín, Rafael, Pombo, Albino, Moreu, Jaime, 2020. An evaluation of the effect that motions at the nacelle have on the cost of floating offshore wind turbines. In: Offshore Technology Conference. Offshore Technology Conference.

Tayfun, M. Aziz, 1980. Narrow-band nonlinear sea waves. J. Geophys. Res. Oceans 85 (C3), 1548–1552.

Tayfun, M. Aziz, Fedele, Francesco, 2007. Wave-height distributions and nonlinear effects. Ocean Eng. 34 (11–12), 1631–1649.

Taylor, Paul H., Jonathan, Philip, Harland, Léon A., 1997. Time domain simulation of jack-up dynamics with the extremes of a Gaussian process. J. Vib. Acoust..

Toffoli, A., Bitner-Gregersen, E., Onorato, M., Babanin, A.V., 2008. Wave crest and trough distributions in a broad-banded directional wave field. Ocean Eng. (ISSN: 0029-8018) 35 (17), 1784–1792. http://dx.doi.org/10.1016/j.oceaneng.2008.08.010.

Toffoli, A., Waseda, T., Houtani, H., Cavaleri, L., Greaves, D.M., Onorato, M., 2015. Rogue waves in opposite currents: an experimental study on deterministic and stochastic wave trains. J. Fluid Mech..

Tromans, P.S., Anaturk, A.R., Hagemeijer, Paul, 1991. A new model for the kinematics of large ocean waves-application as a design wave. In: The First International Offshore and Polar Engineering Conference. International Society of Offshore and Polar Engineers.